JOURNAL OF EXPERIMENTAL AND THEORETICAL PHYSICS, 2024, Vol. 166, No. 6 (12), pp. 777–794

SOLIDS AND LIQUIDS

# QUASI-TWO-DIMENSIONAL ORGANIC CONDUCTOR $\kappa$-(BEDT-TTF)$_2$Cu[N(CN)$_2$]Cl. CONFORMATIONAL DISORDER AND CHARGE STRUCTURE OF CONDUCTING LAYERS

© 2024 A. V. Kuzmin[a,b]*, E. I. Khasanova[a], K. P. Meletov[a], V. N. Zverev[a], S. S. Khasanov[a,b]

[a] Osipyan Institute of Solid State Physics, Russian Academy of Sciences , Chernogolovka, 142432 Russia

[b] National Research University "Higher School of Economics" , Moscow, 119048 Russia

*e-mail: kuzminav@issp.ac.ru

Received April 06, 2024

Revised July 15, 2024

Accepted July 19, 2024

**Abstract**. Using X-ray diffraction analysis (XRD), Raman spectroscopy (RS), and quantum chemical calculations, the features of temperature behavior of thermally activated conformational disorder of terminal ethylene groups $C_2H_4$ of BEDT-TTF (or ET) molecules in crystals of quasi-two-dimensional organic conductor $\kappa$-(BEDT-TTF)$_2$Cu[N(CN)$_2$]Cl were studied at temperatures from 112 K to 289 K. During slow cooling at a rate of –4 K/hour and steps of 10 K, crystal lattice parameters were measured and complete structural analysis was performed for characteristics temperatures. Crystal structure parameters show anomalous temperature behavior in the interval 175–250 K, in the same region an anomaly is observed in the behavior of intramolecular vibration frequencies of the ET molecule, which is associated with changes in the degree of conformational disorder. Based on the obtained structural data, the influence of the observed disorder on the electronic structure of the conducting layer was analyzed using quantum chemical modeling methods. In particular, the results of calculations using the semi-empirical extended Hückel method with a basis set optimized for the given system allowed determining the nature of electron density distribution both within the dimer and within the layer depending on the configuration of terminal ethylene groups. The main types of charge redistribution between molecules in the dimer $ET_2$ were identified. It is shown how the population of configurations and the degree of dimer polarization affect the stability of different types of charge ordering within the conducting layer and, ultimately, the conductive properties of the crystal.

**DOI:** 10.31857/S0044451024120046

## 1. INTRODUCTION

Metallic conductivity in low-dimensional organic crystals based on planar $\pi$-conjugated BEDT-TTF (or ET) molecules is achieved through their specific crystal structure: layered arrangement of donor molecules [1] with relatively large overlap of frontal molecular orbitals (MO). Due to strong interaction between neighboring molecules, narrow energy bands of electronic states can form in such layers. Donor layers typically alternate with layers of strong acceptor anions, which take some electrons from the donor layer. As a result of such charge redistribution, the upper band becomes partially filled, and a metallic state can be realized. Electrons localized in the anion layer do not participate in conductivity, while the current carriers are electrons from donor layers. This type of conductivity has a quasi-two-dimensional character [2], and the anisotropy of conductivity along and across layers is $10^3$–$10^4$.

In the broad class of ET-conductors, the metallorganic salt $\kappa$-(BEDT-TTF)$_2$Cu[N(CN)$_2$]Cl stands out for its non-trivial physicochemical properties. The compound can be obtained in two phase states: Mott insulator (phase κ-Cl) and the so-called κ′-Cl phase – a metal under normal conditions, which transitions to a superconducting state at $T_c = 11.5$ K [3]. Crystals κ-Cl and κ′-Cl have similar layered structure [4], where ET molecules in the conducting layer dimerize and form a triangular lattice, which is

characteristic of the $\kappa$-phase. One of the remarkable properties of $\kappa$-(BEDT-TTF)$_2$Cu[N(CN)$_2$]Cl crystals is the abrupt change in resistance depending on the applied voltage, which can be used for creating logic elements based on them [5].

The physicochemical properties of salt $\kappa$-(BEDT-TTF)$_2$Cu[N(CN)$_2$]Cl strongly depend on the details of the internal structure of cationic and anionic layers. It is assumed that conductivity is related to the structural disorder in ethylene groups $-C_2H_4-$ of ET molecules [5], which can affect the distribution of electron density concentrated on ET. This, in turn, is a prerequisite for the emergence of exotic states of "crystal with paired electrons" or "quantum dipole crystal" [6] and "quantum dipole liquid" [7]. The disorder $-C_2H_4-$ is believed to have a thermoactivated nature and vitrifies at temperatures around 70 K [8, 9, 10]. Obviously, the ordering of ethylene groups is a classical relaxation process, and the associated physicochemical properties of the object are due to kinetic effects and depend on cooling/heating rates. Such phenomena are often observed in van der Waals crystals of "mobile" macromolecules, particularly fullerites –crystals of quasi-spherical fullerenes $C_{60}$, where kinetic effects are quite pronounced [11,12]. In the case of κ-phases, these issues are poorly covered, especially from a structural perspective, and the superficial description of configurational disorder in published structures $\kappa$-(BEDT-TTF)$_2$Cu[N(CN)$_2$]Cl only confirms this conclusion.

The aim of this work is to fill the gap in studying ordering processes in crystals $\kappa$-(BEDT-TTF)$_2$Cu[N(CN)$_2$]Cl, which are so important for predicting their functional properties. Based on structural data collected over a wide temperature range, the temperature behavior of disorder in ET ethylene end groups was studied, and quantum chemical calculations were performed, taking into account partial activation of various group configurations in the conducting layer. The calculation results allowed drawing conclusions about the relationship between ET configurational instability and the charge structure of the layer, which cannot be detected by standard X-ray diffraction analysis methods alone.

## 2. EXPERIMENTAL PART

Crystals $\kappa$-(BEDT-TTF)$_2$Cu[N(CN)$_2$]Cl were obtained by electrocrystallization according to the previously described method [13]. High-quality samples with good faceting were studied by single-crystal X-ray diffraction analysis (XRD) using a Gemini R Rigaku-Oxford Diffraction laboratory diffractometer and $K_\alpha$Mo radiation. The diffractometer is equipped with a fourcircle goniometer in $\kappa$-geometry, a two-coordinate Atlas S2 CCD detector, and a Cryojet flowtype cryogenic attachment from Oxford Instruments. Structural models of the studied samples were obtained by direct methods using SHELXT program and refined by full-matrix least squares method in SHELXL program (both included in the SHELX software package [14, 15]). Non-hydrogen atom parameters were refined in anisotropic approximation. Hydrogen atom positions were found geometrically and refined in isotropic approximation with constraints $U_{iso} = 1.2U_{eq}$, where $U_{eq}$ — equivalent thermal parameters of the carbon atom to which the hydrogen atom is directly bonded.

Calculations of electronic characteristics of the periodic system were performed within the framework of Extended Hückel Theory (EHT) using an unbiased grid of special $k$-points with density $7 \times 2 \times 7$, constructed according to the Monkhorst-Pack scheme [16]. For refinement of EHT parameters in ORCA program [17], quantum-chemical modeling of the electronic spectrum of isolated dimers was performed using Density Functional Theory (DFT) and hybrid functional B3LYP with basis set 6-31G [18].

Raman spectra were obtained in the backscattering geometry using an Acton SpectraPro-2500i spectrograph with a Pixis 2K detector (operating temperature CCD matrix mode is about $-70^\circ$C) and an Olympus BX51 microscope. For Raman excitation, a continuous-wave diode-pumped solid-state laser with power up to 100 mW and wavelength $\lambda = 532$ nm was used along with an edge filter for this wavelength with a bandwidth of about 60 cm$^{-1}$. The laser beam was focused on the sample using an Olympus objective 50× into a spot with a diameter of about 1.3 μm. Temperature control was maintained using a nitrogen cryostat with cold sample loading, equipped with a temperature controller based on a resistive heater, TERMODAT-08M3 temperature controller, and SB10M3 power unit.

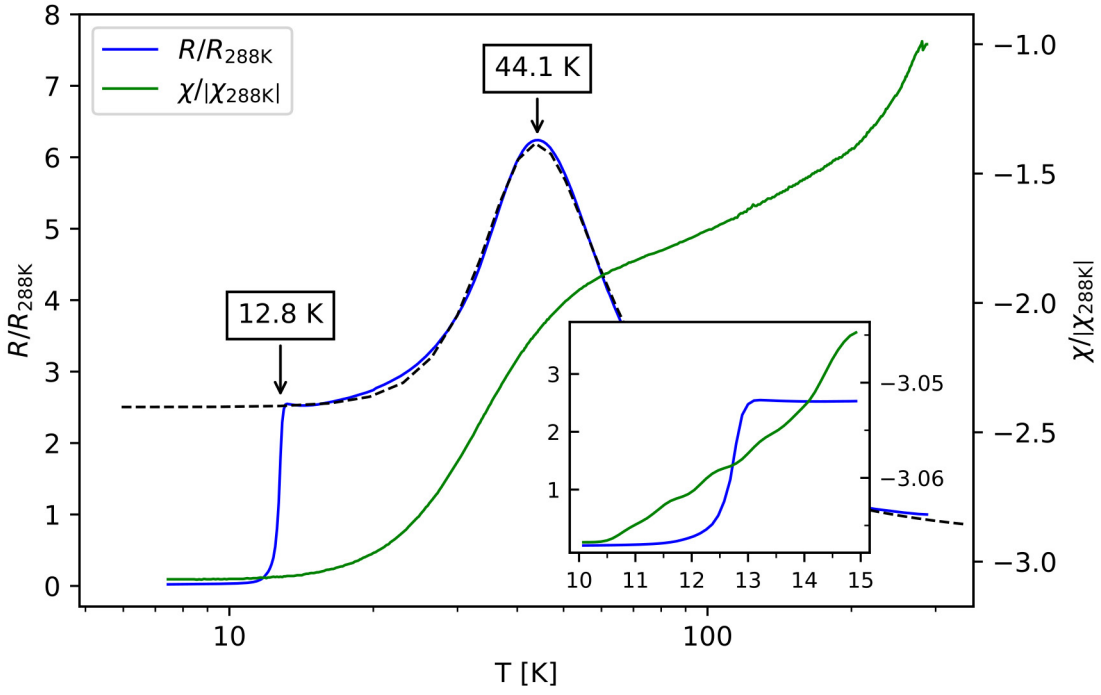


**Fig. 1.** Graph of normalized transverse resistance measurements $R/R_{288K}$ $\chi/\chi_{288K}$ ($R_{288K}$ and $\chi_{288K}$ — resistance and magnetic susceptibility at corresponding temperatures) of crystals $\kappa$-(BEDT-TTF)$_2$Cu[N(CN)$_2$]Cl (phase $\kappa'$-Cl)

Temperature dependencies of transverse resistance were obtained using four-point magnetoresistance measurement technique with a probe current of 1 mA. Flat, well-faceted crystals with dimensions $0.5 \times 0.1 \times 0.5$ mm$^3$, previously subjected to X-ray analysis, were selected for measurements.

## 3. RESULTS AND DISCUSSION

### 3.1 Crystal Testing $\kappa$-(BEDT-TTF)$_2$Cu[N(CN)$_2$]Cl

As mentioned earlier, the compound $\kappa$-(BEDT-TTF)$_2$Cu[N(CN)$_2$]Cl can be synthesized in two different states: phases κ-Cl and κ′-Cl. The first is a Mott insulator, while the latter exhibits metallic properties with a transition to superconducting state at temperatures 11.3–11.9 K and normal pressure [4]. Both phases have similar crystal lattice parameters and identical structure up to disorder in the terminal ethylene groups of ET. To determine which phase our crystals $\kappa$-(BEDT-TTF)$_2$Cu[N(CN)$_2$]Cl belong to, magnetoresistance measurements were conducted. Temperature dependence of magnetic susceptibility and relative resistance across conducting layers are shown in Fig. 1. They were obtained under normal pressure and cooling rate 120 K/ч.

From the transverse resistance plot $R/R_{288K}(T)$ it follows that the used crystals $\kappa$-(BEDT-TTF)$_2$Cu[N(CN)$_2$]Cl undergo a smooth transition to the superconducting state at a temperature of about 12.8 K. At the same time, there is no apparent jump in the magnetic susceptibility curve $\chi/\chi_{288K}(T)$ (see inset in Fig. 1), which is not typical for this family of compounds. The temperature range of the "smeared" phase transition is close to that previously reported for crystals κ′-Cl, although it occurs several degrees higher relative to the known metal ↔ superconductor transformation temperatures for the latter.

The reason for such behavior $R$ and $\chi$ is not entirely clear and possibly related to the effect of partial shunting by superconducting domains, in case only certain regions of the sample undergo phase transformation. This forms a superconducting cluster that "nullifies" the sample resistance, but the superconducting phase fraction is insufficient for generating circular currents that expel magnetic flux. The second critical point is the temperature of 44.1 K, at which the character of the temperature dependence of resistance changes. In literature,

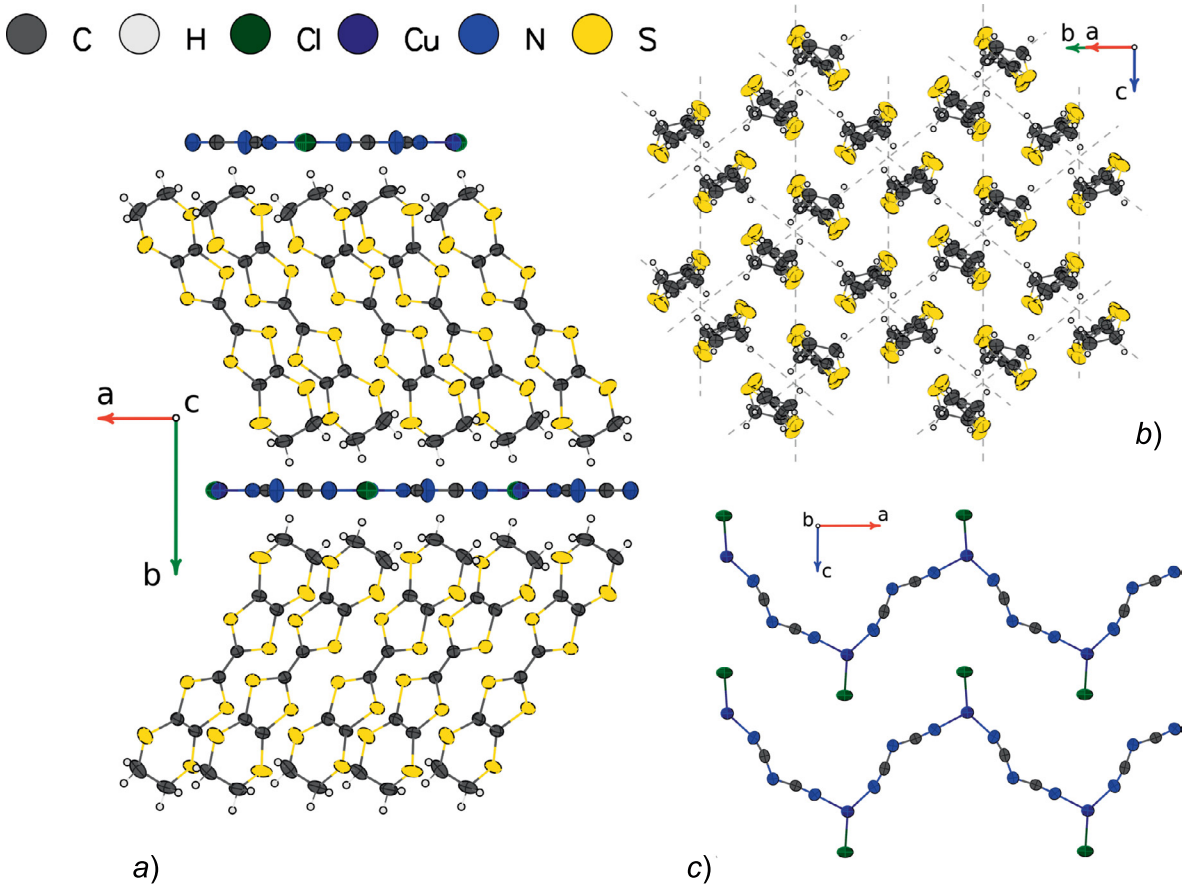


**Fig. 2.** Layered structure of $\kappa$-(BEDT-TTF)$_2$Cu[N(CN)$_2$]Cl (*a*); cationic conducting layer (*b*); anionic insulating layer (*c*)

it is commonly referred to as the Brinkman-Rice temperature ($T_{BR}$) and associated with a metal-to-semiconductor crossover transition [19]. Approximation of the resistance curve by the sum of metallic [20] and Boltzmann parts of temperature dependencies

$$R^{-1} = R_m^{-1} + R_s^{-1},$$

where $R_m = R(0) + AT^n$, and $R_s = R_0 \exp\left(E_g / 2k_B T\right)$, gives activation energy $E_g = 243.7$K and power exponent $n = 5.54$. The latter value is close to theoretical for simple metals [21]. Collectively, the presence of superconducting transition and metallic state at atmospheric pressure allows us to assert that our samples $\kappa$-(BEDT-TTF)$_2$Cu[N(CN)$_2$]Cl are closer in electronic properties to $\kappa'$-phase than to the known Mott insulator $\kappa$-Cl.

Structural data were obtained on a well-faceted crystal $\kappa$-(BEDT-TTF)$_2$Cu[N(CN)$_2$]Cl with linear dimensions of about 200 μm in the temperature range from 112 K to 289 K. Unit cell parameters were refined during a multi-temperature experiment with a step of 10 K, and at temperatures of 112 K, 147 K, 194 K, and 289 K, complete X-ray diffraction experiments were conducted followed by XRD analysis. The effective cooling rate, taking into account stops for six-hour experiments, was −4 K/h. Thus, we collected high-resolution structural data with reliability factors $R_1 \leq 5\%$, allowing the application of computational semi-empirical methods.

Structure models $\kappa$-(BEDT-TTF)$_2$Cu[N(CN)$_2$]Cl with varying degrees of accuracy were previously described in works [22, 23]. The crystals have a layered structure with alternating conducting cationic and insulating anionic layers (see Fig. 2*a*). The crystal structure is orthorhombic P*mna* with unit cell parameters $a = 12.9457(6)$ Å, $b = 29.8856(13)$ Å, $c = 8.4576(3)$ Å and volume $V = 3272.2(2)$ Å$^3$ at room temperature. The main structural unit of the conducting cationic layer are dimers of donor BEDT-TTF or ET molecules (see Fig. 2*b*), packed in a triangular lattice. The flat

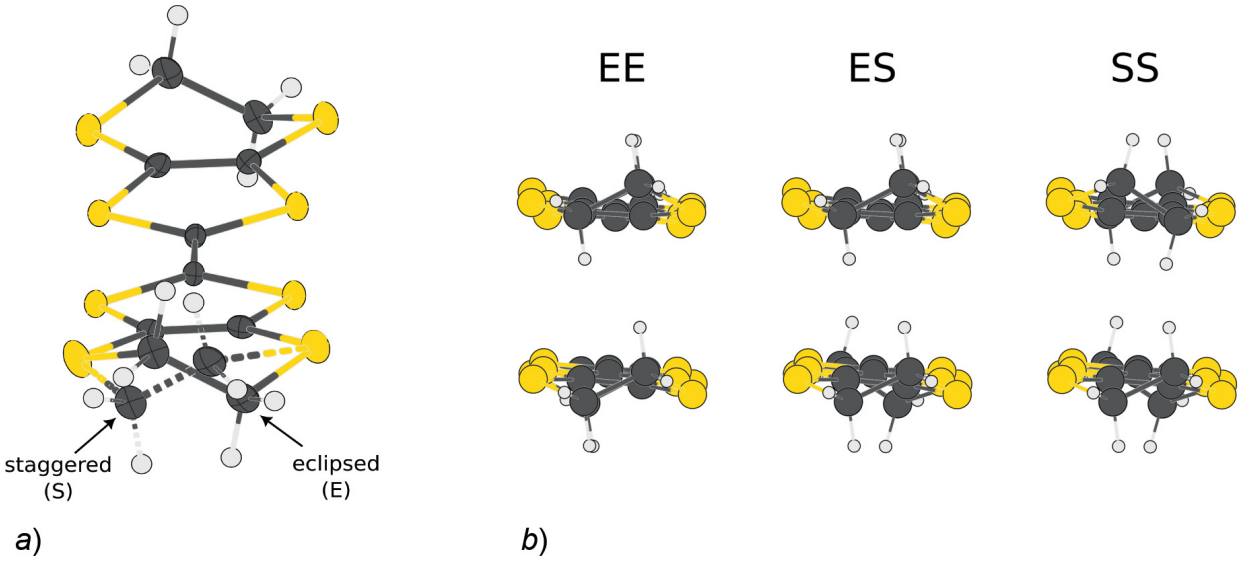


**Fig. 3.** Two configurations of ethylene groups of ET molecules: staggered (S) and eclipsed (E) (*a*), possible dimer configurations $ET_2^+$: EE – eclipsed-eclipsed, ES – eclipsed-staggered, SS – staggered-staggered (*b*)

BEDT-TTF molecule is a heterocycle consisting of eight sulfur atoms and ten carbon atoms. The edges of the molecule are closed by particularly mobile terminal ethylene groups $-CH_2-CH_2-$, extending beyond the molecular plane. It is believed that the sulfur atoms in ET "strengthen" the dimer layer, as they contribute to the formation of a network of intermolecular S···S contacts, while ethylene groups, on the contrary, hinder $\pi$-interaction of molecules. The anionic layer consists of zigzag chains of anions Cu[N(CN)$_2$]Cl, stretched along the crystallographic direction *a*. The anion Cu[N(CN)$_2$]Cl includes $Cu^{1+}$, atoms connected to two dicyanoamide groups $[(NC)N(CN)]^-$ and a terminal Cl atom (see Fig. 2*c*).

In crystals of $\kappa$-(BEDT-TTF)$_2$Cu[N(CN)$_2$]Cl, as in most similar compounds with ET, the terminal ethylene groups $-C_2H_4-$ of one of the six-membered rings of ET molecules are prone to structural disorder. At room temperature, these groups occupy two positions with probabilities of 0.8 and 0.2. In structural analysis, these probabilities are typically characterized by a parameter called the atomic site occupancy. In structures with disorder, the atomic occupancy values are optimized during the refinement of the structural model. The more probable molecular configuration (with the highest occupancy of the $-C_2H_4-$ group) is called eclipsed (E), while the less probable one is called staggered (S) (see Fig. 3*a*). By its nature, the disorder of ethylene groups is dynamic, and the ratio of E : S occupancies changes depending on temperature. Taking into account the two configurations of the $-C_2H_4-$ group, three types of dimers can be formed: EE, when both monomers are in E configuration, SS – both monomers in S configuration, and ES for mixed dimers (see Fig. 3*b*).

On the temperature dependence of cell parameters (see Fig. 4*a*) a feature is visible in the temperature range from 175 K to 250 K, expressed in the change of slope of temperature dependencies. For example, on the unit cell volume curve, there is a sharp drop in its values, while in the high-temperature region $V(T)$ decreases with temperature according to the quadratic law

$$V(T) = \beta(T)T + 3202.8,$$

where the coefficient of volumetric thermal expansion $\beta$ linearly depends on temperature:

$$\beta(T) = 9.27 \cdot 10^{-4} T + 0.018.$$

After passing through the anomalous region and a small plateau around $T = 160$ K, the rate of temperature dependence decline recovers, and the curve $V(T)$ continues to decrease quadratically. Approximation of the volume curve $V(T)$ in the low-temperature region gives the equation

$$V(T) = \beta(T)T + 3187.7,$$

where

$$\beta(T) = 9.47 \cdot 10^{-4} T + 0.065.$$

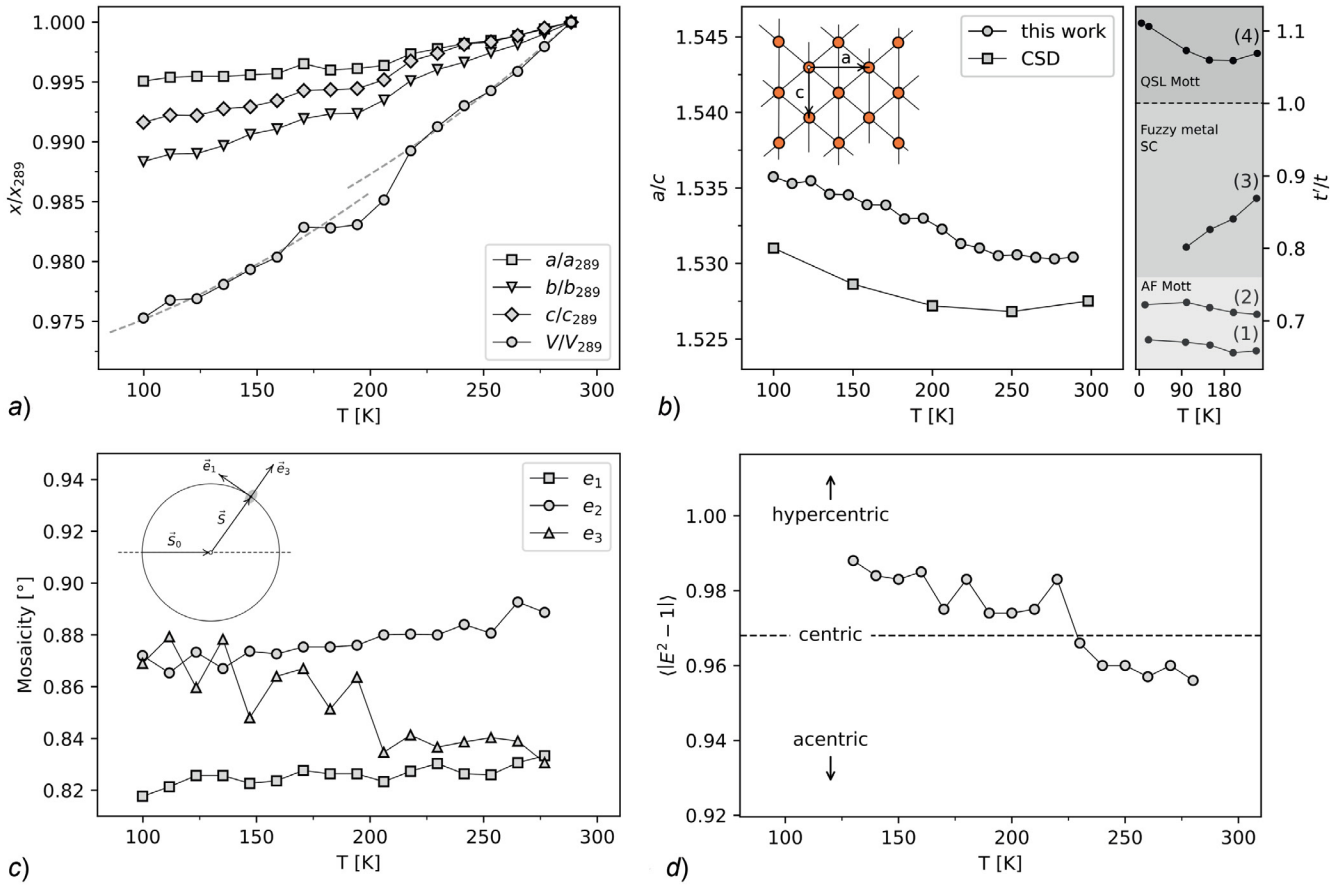


**Fig. 4.** Temperature behavior of cell parameters of crystals to $\kappa$-(BEDT-TTF)$_2$Cu[N(CN)$_2$]Cl (*a*), ratio of parameters *a*/*c* (CSD — data on pure $\kappa$-phase from Cambridge database [9]) and calculated values of transfer integral ratios $t'/t$ for $\kappa$-(BEDT-TTF)$_2$Cu[N(CN)$_2$]Br — *1*, $\kappa$-(BEDT-TTF)$_2$Cu[N(CN)$_2$]Cl — *2*, $\kappa$-(BEDT-TTF)$_2$Cu(NCS)$_2$ — *3*, $\kappa$-(BEDT-TTF)$_2$Cu(CN)$_3$ — *4* according to [9] (b), temperature dependence of mosaicity parameters $e_1$, $e_2$ and $e_3$ of crystal $\kappa$-(BEDT-TTF)$_2$Cu[N(CN)$_2$]Cl (designations $\vec{S}_0$ and $\vec{S}$ on the simplified scheme of diffraction experiment show directions of incident and diffracting X-ray beam) (c), moments $\langle|E^2-1|\rangle$ of distributions of normalized experimental structure amplitudes $E = |F|^2/\langle|F|^2\rangle$ according to [30] (d)

According to the approximating equations, the difference between two temperature regions is mainly manifested in the values of temperature-independent constants $V(T)$: 3202.8Å$^3$ and 3187.7Å$^3$ respectively for temperatures above and below.

From the perspective of electron interaction in the cationic layer, an interesting parameter is the ratio *a*/*c*, as it directly affects the values of transfer integrals $t'$ and $t$ between dimers in the layer [24]. In an ideal isotropic triangular lattice $a/c = \sqrt{3} \approx 1.732$. In Fig. 4*b*, it can be seen that above $T = 200$ K the ratio *a*/*c* changes slightly near 1.531, however, below this temperature, the processes of "isotropization" of the triangular lattice begin – the value *a*/*c* slowly increases, although it still remains less than $\sqrt{3}$. When comparing the values *a*/*c* for the $\kappa'$-phase with literature data for pure κ-phase, published in the Cambridge Structural Database (CSD), it is evident that both dependencies increase with decreasing temperature. Moreover, the ratio *a*/*c* in $\kappa'$ is greater than that in the κ-phase throughout the entire temperature range up to 100 K. In general, the value of the ratio *a*/*c* correlates with the ratio in the two-dimensional layer $t'/t$ and its increased value may explain why, unlike the Mott insulator κ-Cl, $\kappa'$-phase is a metal under normal conditions and is similar in conductive properties to $\kappa$-(ET)$_2$CuNCS)$_2$ [9].

Figure 4*c*,*d* shows the results of preliminary processing of diffraction data from a series of low-temperature experiments. Figure 4*c* shows the temperature behavior of mosaic parameters: the width of the diffraction spot in degrees in the

directions of the internal orthogonal coordinate system of reflection $\{\vec{e}_1,\vec{e}_2,\vec{e}_3\}$ — a generally accepted measure of sample diffraction quality in single crystal analysis [25]. The coordinate system $e_i$ is introduced in such a way that vectors $\vec{e}_1$, and $\vec{e}_2$ are tangential to the Ewald sphere, and vector $\vec{e}_3$ is perpendicular to the sphere surface (see inset in Fig. 4*c*), i.e., approximately corresponds to the direction of reciprocal space scanning [26,27]. With such definition of the basis set, the mosaic value $e_3$ is analogous to rocking curve profiles. It can be seen that during slow cooling of the sample, the mosaic parameters $e_1$ and $e_2$ slowly decrease, as expected due to the general decrease in the amplitude of thermal vibrations of atoms. However, the angular size of the diffraction spot along $e_3$ behaves non-monotonically. Until 200 K, it maintains some average value close to $e_1$ but with further cooling, it sharply increases in magnitude. The increase in the mosaic parameter – the angular size of the diffraction spot, indicates changes in the microstructure of coherent scattering regions [28,29] (domains) and is interpreted as an increase in the spread of domain lattice parameter values and/or angular misorientation of domains.

The behavior of the temperature dependence of the statistical distribution of experimental intensities $|F|^2$ is of interest. Fig. 4*c* shows the temperature dependencies of shifted moments $\langle|E^2-1|\rangle$ of normalized integral intensities $E=|F|^2/\langle|F|^2\rangle$ for several temperatures, as well as the exact theoretical values of moments for centrosymmetric, non-centrosymmetric, and hypercentrosymmetric crystallographic systems [30]. According to the intensity statistics, the crystallographic system is close to centrosymmetric; however, in the region of relatively high temperatures (up to 225 K), the moments $\langle|E^2-1|\rangle$ lie below their theoretically expected values. During further cooling, the moments sharply increase in magnitude and enter the region expected for hyper centrosymmetric systems, although they are quite far from the corresponding theoretical values. The hypercentrosymmetry of the system indicates the presence of additional inversion centers in the symmetrically independent part of the crystal cell (basis). In the structure of $\kappa$-(BEDT-TTF)$_2$Cu[N(CN)$_2$]Cl the basis contains one ET molecule, which, as described above, exists in two configurations E or S with a total occupancy of 1.0 (see Fig. 3*a*). If tests for the presence of point group symmetry elements are conducted for each configuration, it turns out that for the group $C_i$ the root-mean-square deviations of atomic positions from symmetric ones (or $R(C_i)$) in the case of configuration E equals 0.366, which is almost twice less than for configuration S, for which $R(C_i)=0.583$. The observed tendency of $\langle|E^2-1|\rangle$ values to shift towards "hypercentrosymmetric" values apparently may be related to the increase in the proportion of E configurations during slow cooling of the sample.

The set of observed structural phenomena indicates that the causes of temperature features in the range from 175 K to 250 K may be associated with dynamic disorder of configurations E $\leftrightarrow$ S. It is interesting to compare the behavior of structural parameters with the results of other methods more sensitive to vibrational motion –$C_2H_4$–. In particular, of interest are measurements of temperature-normalized times $^1$H of spin-lattice relaxation $(T_1T)^{-1}$ as a result of processing a series of nuclear magnetic resonance spectra (NMR) in a magnetic field directed perpendicular to the conducting layers of crystals $\kappa$-(BEDT-TTF)$_2$Cu[N(CN)$_2$]Cl [31]. In the original work, the authors do not specify which samples are being discussed, but most likely, the measurements were conducted on the pure phase $\kappa$-Cl. The measurements show that two distinct maxima stand out on the graphs $(T_1T)^{-1}$. The formation of the first broad maximum near $T=280$ K begins with a sharp increase in inverse relaxation times above $T=200$ K, which the authors explain by thermoactivated oscillations of ethylene groups and provide estimates of activation energy $2600\pm100$ K. Considering that the intensities of such atomic oscillations decrease exponentially with temperature, the authors associate the second sharp maximum at $T=50$ K with phenomena of purely electronic nature and magnetic transitions. The authors identify 162 K as the boundary below which thermal effects in groups –$C_2H_4$– weaken. In the wide interval from 160 K to the sharp peak around 27 K, the NMR spectra structure remains practically unchanged, and the boundary temperature itself corresponds to the lower elongated minimum on the temperature dependence $(T_1T)^{-1}$. Notably, in some isostructural compounds, namely $\kappa$-(BEDT-TTF)$_2$Cu[N(CN)$_2$]Br, data reveal

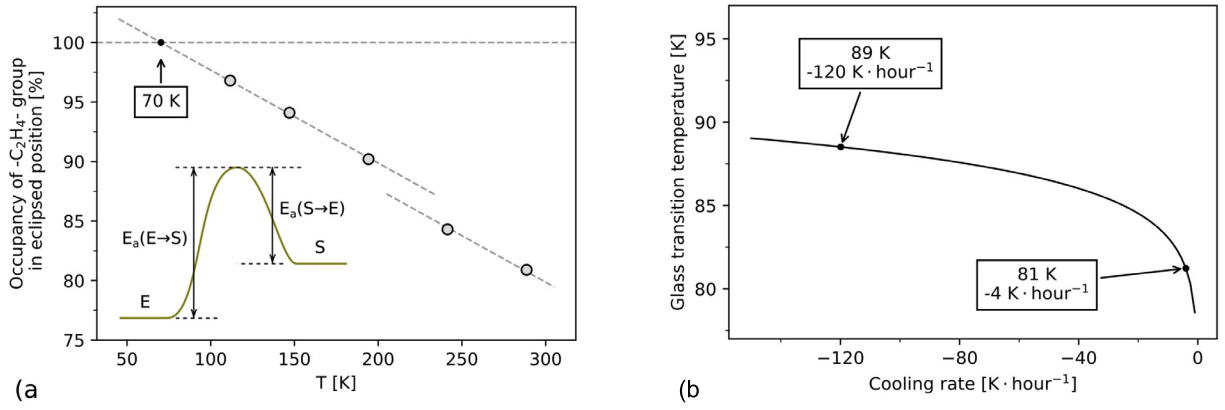


**Fig. 5.** Population of E-configuration of ethylene tails of ET molecules depending on temperature in to $\kappa$-(BEDT-TTF)$_2$Cu[N(CN)$_2$]Cl (*a*), theoretical dependence of glass transition temperature on cooling rate for $\kappa$-(BEDT-TTF)$_2$Cu[N(CN)$_2$]Br (*b*)

anomalies around the same temperature — 160 K, which is commonly associated with the formation of an incommensurate structure from partially ordered ethylene layers [32–34].

### 3.2. Disorder in the cation layer

Detailed crystal chemical analysis of structural data allowed to establish the temperature behavior of disorder parameters in terminal ethylene groups of ET molecules (Fig. 3*a*). Temperature dependencies of the occupancy parameter of ethylene groups (see Fig. 5*a*) monotonically approach 100%, so that the expected complete ordering in the structure of the cation layer can be achieved at temperatures close to $T_{BR}$. Linear extrapolation of the temperature dependence of occupancy to low temperatures indicates complete stabilization of ethylene groups in E-configuration at a temperature of about 70 K. It should be noted that at low temperatures, the phenomenon of disorder glass formation is also possible, which is often referenced in literature [8, 35, 36]. During glass formation, the occupancy curve will gradually reach a plateau after $T = 70$ K, which means preservation of residual occupancy of the minor position of ethylene groups (S-configuration). Determination of such small occupancy values by X-ray structural methods is problematic, and the study of such processes requires more sensitive experimental approaches and methods.

The relatively low ordering/glass formation temperature distinguishes $\kappa$-(BEDT-TTF)$_2$Cu[N(CN)$_2$]Cl from other $\kappa$-salts, particularly from $\kappa$-(BEDT-TTF)$_2$Cu$_2$(CN)$_3$, where structurally visible ordering occurs around 130–150 K. Fig. 5*b* shows the dependence of glass formation temperature $T_g$ on cooling rate $r_c$ according to the theoretical model of a system with two states separated by a temperature-independent energy barrier (see inset in Fig. 5*a*) [8,37].

A consequence of the model proposed by the authors is the relationship between $T_g$ and $r_c$ through equation

$$\frac{T_g^2}{|r_c|}\frac{k_B}{E_a} = \nu_0^{-1}\exp\left(\frac{E_a}{k_B T_g}\right).$$

For the isostructural salt $\kappa$-(BEDT-TTF)$_2$Cu[N(CN)$_2$]Br taking into account the parameters determined by the authors

$$E_a(\mathrm{S} \rightarrow \mathrm{E}) = E_a = 3200 \pm 300 \text{ K},$$

$$\nu_0 = 5.0 \cdot 10^{15\pm1.5} \text{ Hz}$$

the equation gives glass formation temperature dependence $T_g(|r_c|)$ with accuracy ±15.6K. This simplified theoretical model predicts that increasing $r_c$ by almost 30 times shifts $T_g$ only by 8 K, therefore strong differences in ordering/glass formation temperatures of $\kappa$-salts are mainly related to the structural features of each individual compound, rather than changes in cooling/heating rates.

In general, the population of the E-configuration $O(T)$ changes in the studied temperature range almost linearly with a rate of

$$dO(T)/dT = -7.8 \cdot 10^{-4}\,\mathrm{K}^{-1}.$$

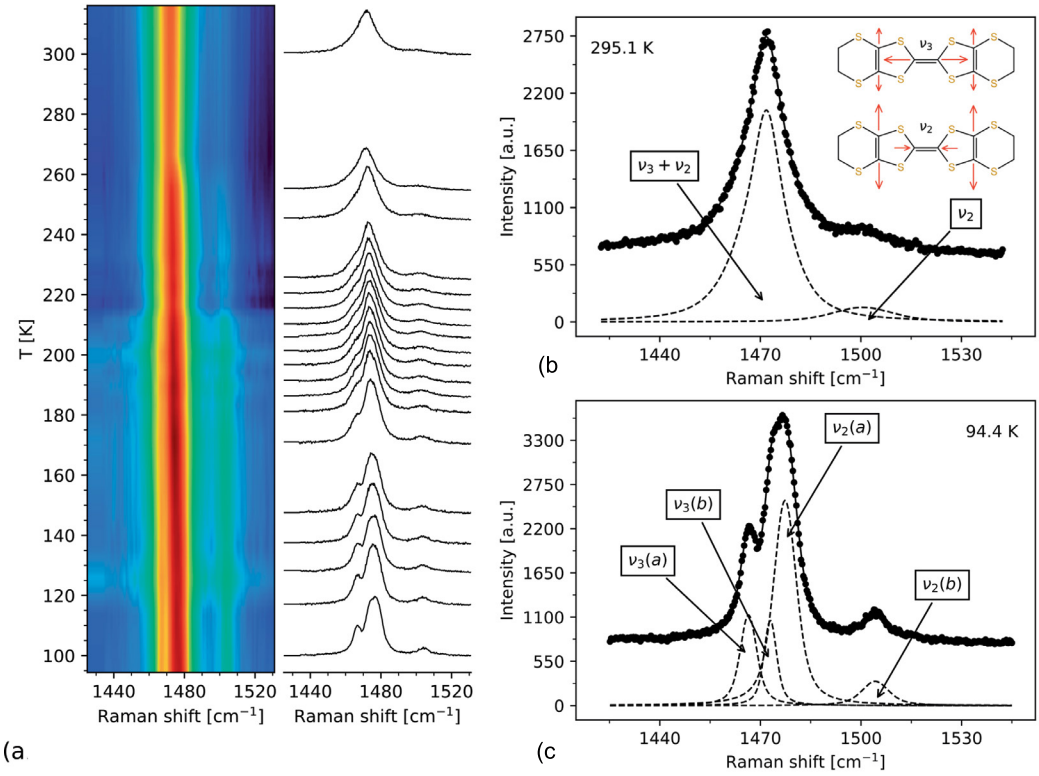


**Fig. 6.** Raman scattering spectra for crystals $\kappa$-(BEDT-TTF)$_2$Cu[N(CN)$_2$]Cl (*a*), peak decomposition of characteristic modes in the range 1410–1530 cm$^{-1}$ for high and low temperatures (*b, c*)

At temperatures around 200 K, a small bend is observed on the graph, associated with an abrupt change in the temperature-independent part $O(T)$. Its position correlates with the features detected on the graphs of cell parameters and statistical curves (see Fig. 4), which indicates the commonality of their underlying causes.

### 3.3. Optical properties of crystals $\kappa$-(BEDT-TTF)$_2$Cu[N(CN)$_2$]Cl

To confirm the connection between thermoactivation "switches" E ↔ S with non-trivial

behavior of structural characteristics of crystals $\kappa$-(BEDT-TTF)$_2$Cu[N(CN)$_2$]Cl in the range from 175 K to 250 K, we conducted a series of multi-temperature optical studies using Raman spectroscopy. Special attention was paid to the spectral frequency range of 1410–530 cm$^{-1}$ where intramolecular vibrational modes of individual ET molecules are located [38].

Raman spectra of crystals $\kappa$-(BEDT-TTF)$_2$Cu[N(CN)$_2$]Cl were measured at 19 different temperatures in the range from 94 K to 295 K, the results of their processing are presented in Fig. 6. In low-temperature spectra (see Fig. 6*b*), three peaks are clearly visible, with the central peak shape being asymmetric, suggesting its doublet structure. According to literature data, frequencies in this range correspond to normal vibrational modes $\nu_3$ and $\nu_2$ of ET monomers [38, 39]. The mode type $\nu_3$ corresponds to vibrations of the central double bond C = C of the ET molecule, and the mode $\nu_2$ — to symmetric vibrations of double carbon bonds from the peripheral five-membered rings of the molecule (see inset Fig. 6*b*). The shift in the position of mode $\nu_2$ is often used as a marker of the charge state of ET because its position is sensitive to the molecule's charge and linearly depends on its magnitude [38, 40, 41]. Additionally, the bands of corresponding modes tend to split into two or more components if charge inhomogeneities of ET are present in the crystals.

Overall, the spectral pattern observed for samples $\kappa$-(BEDT-TTF)$_2$Cu[N(CN)$_2$]Cl is typical for ET compounds. At high temperatures, the spectrum in the region of 1410 cm$^{-1}$–1530 cm$^{-1}$ consists of two broad maxima, one of which corresponds to the

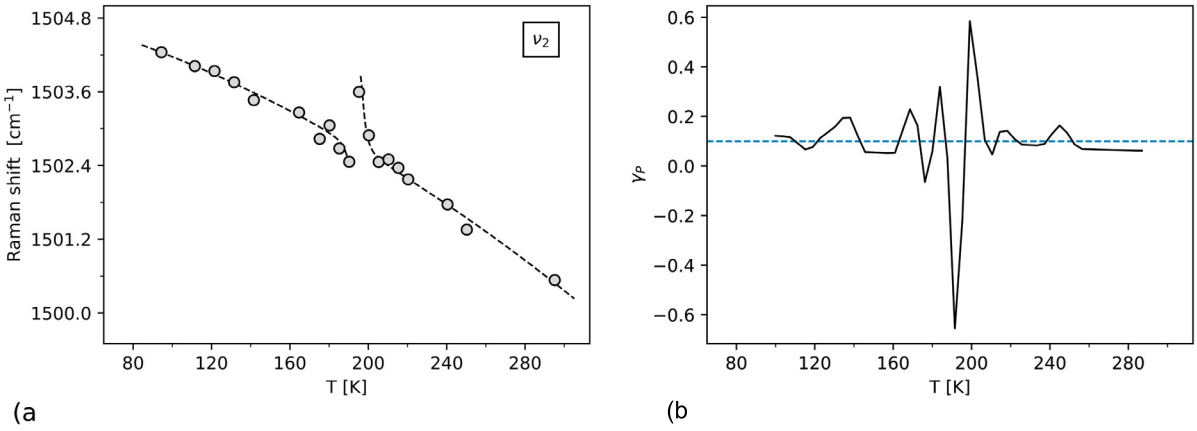


**Fig. 7.** Temperature dependence of mode shift $\nu_2$ (*a*), values of the Grüneisen parameter $\gamma_P(T)$ (*b*)

frequencies of mode $\nu_2$, while the other, according to literature data, is formed mainly from the band of mode $\nu_3$ with a possible admixture of the second component $\nu_2$ (see Fig. 6*b*). The spectrum remains practically unchanged until approximately 260 K, and upon further cooling, the intense maximum becomes asymmetric. The asymmetry increases with decreasing temperature and leads to its triple splitting at $T = 94$ K (see Fig. 6*c*). The three components of the former broad maximum are identified as overlapping peaks of modes $\nu_3(a)$, $\nu_3(b)$ and $\nu_2(a)$, where $a, b$ denotes new components after splitting. The observed bifurcation of modes $\nu_3$ and $\nu_2$ indicates that the charge inhomogeneity of ET molecules persists over a wide temperature range.

Let's examine in detail the single maximum $\nu_2$ with a frequency of about 1500 cm$^{-1}$ in the high-energy region of the spectrum. The maximum barely changes at high temperatures, remaining small in magnitude, but below $T = 200$ K its intensity increases and it acquires a more distinct contour. Overall, with cooling, the frequency of mode $\nu_2$ smoothly increases, however, strongly deviates from the monotonic dependence and shows singularity in the region of 175–200 K with an initial jump towards higher values (see Fig. 7*a*). The sharp jump in the oscillation frequency of mode $\nu_2$ agrees well with nuclear magnetic resonance data [31], according to which the graphs of $^1$H spin-lattice relaxation times show a maximum associated with thermoactivated oscillations of ethylene groups [31].

In addition to the explicit splitting of mode maxima $\nu_2$, their shift in the spectrum is also a marker of changes in the charge state of the ET molecule [38, 41]. Except for the anomalous zone of 175–200 K, the temperature behavior of the mode caused by compression (expansion) of the crystal lattice can be described by an exponential law

$$\nu_2(T) = \nu_2^0 \exp\left(-\gamma\beta_0 T - \gamma\beta_1 T^2/2\right),$$

obtained by integrating the equation for the temperature-independent single-mode Grüneisen parameter $\gamma$:

$$\frac{1}{\nu_2^0}\frac{d\nu_2}{dT} = -\gamma\beta(T),$$

where $\beta(T) = \beta_0 + \beta_1 T$ [39, 42]. Here $\beta$ represents the thermal expansion coefficient, $\beta_0$ and $\beta_1$ — are the coefficients of its linear temperature dependence, $\nu_2^0$ — is the normalization constant. The approximation of experimental data on the position of maxima $\nu_2$ by the nonlinear least squares method gives the following values of constants:

$$\nu_2^0 = 1505.13\,\text{cm}^{-1}$$

$$\gamma\beta_0 = 4.3072 \cdot 10^{-6}\,\text{K}^{-1},$$

$$\gamma\beta_1 = 4.1804 \cdot 10^{-8}\,\text{K}^{-2}.$$

These parameters are close to those for the pure phase $\kappa$-Cl [39], however, in the latter, no visible changes in the optical spectra were detected [43].

Figure 7*b* shows the temperature dependence graph of the dimensionless single-mode Grüneisen parameter [44]

$$\gamma_P(T) = -\frac{\partial \ln \nu_2}{\partial \ln V},$$

calculated based on experimental X-ray diffraction and optical data: $V(T)$ (see Fig. 4*a*) and $\nu_2(T)$. Parameter $\gamma_P$ combines the results of optical and X-ray diffraction measurements and allows estimating the correction for frequency shift due to thermal expansion (compression) of the crystal lattice. Its value is a measure of anharmonicity of the corresponding vibrational modes of atoms in the crystal. In case the vibrations are harmonic, $\gamma_P$ should be equal or close to zero. In crystals $\kappa$-(BEDT-TTF)$_2$Cu[N(CN)$_2$]Cl the average value of $\gamma_P$ in the temperature range from 94 K to 295 K equals 0.01, while the parameter itself deviates relatively weakly from the average except for the region around 200 K. Such behavior of $\gamma_P$ shows that the frequency value jumps $\nu_2(T)$ in the narrow temperature range around 200 K are exclusively intramolecular in nature. They indicate a nonlinear amplitude forcing force (anharmonicity) of intramolecular vibrations sensitive to the charge of ET-molecule bonds in this temperature range and are not directly related to thermal compression (expansion) of the crystal lattice.

### 3.4. Charge distribution in the $ET_2^+$-layer

The question of the influence of thermal oscillations of terminal ethylene groups of individual ET molecules on the general properties of the conducting layer, directly related to conductivity, metal ↔ superconductor phase transitions, and others, deserves attention. The most accessible approaches for analyzing the electronic spectrum of the system are numerical methods of quantum-chemical modeling based on experimental X-ray diffraction data.

There are several ways to account for the influence of structural disorder in calculations of the electronic spectrum of the system: the virtual crystal approximation [45], the coherent potential approximation [46], and the supercell method. The first two approximations are typically used for modeling inorganic materials (mainly alloys) and have several limitations. The supercell method involves constructing and calculating an ordered cell of larger size (multiple of the original) and averaging the results. Due to its specificity, this approach is very demanding on computational resources; however, when using simplified calculation methods (for example, semi-empirical), it can be combined with the Monte Carlo method for analyzing systems with dynamic disorder, such as the conformational disorder of ethylene groups in the $ET_2^+$-layer.

The extended Hückel method (PMX or EHT) used in this work, being semi-empirical, partially uses experimentally determined fixed parameters in its algorithm. For example, ionization potentials are used as diagonal elements of the Hamiltonian $H_{ii}$. The standard parameters supplied with the YAeHMOP program [47] do not always provide a qualitatively correct picture of the electronic level distribution in the calculated systems. For this reason, to correctly describe the energy spectrum of molecules, it is necessary to optimize the internal parameters of the PMX method. The parameter optimization procedure involved changing them in such a way that the energy spectra of dimers calculated by this method EE, ES and SS best corresponded to similar spectra calculated within the framework of the more rigorous density functional theory (DFT). As a criterion of correspondence, the averaged sum of squares of energy differences of 18 frontal orbitals of dimers was taken

$$\mathrm{RMSD} \propto \sqrt{\sum_{i=\mathrm{HOMO}-9}^{\mathrm{HOMO}+8} \left(E_i^{\mathrm{EHT}} - E_i^{\mathrm{DFT}}\right)^2},$$

which was minimized by the nonlinear least squares method with respect to PMX parameters. The set of variable parameters included pre-exponential and exponential multipliers of Slatertype basis functions (STO) for C, H, S atoms and the Wolfsberg-Helmholtz constant. The results of parameter optimization are shown in the energy spectra diagrams of dimers (see Fig. 8).

For calculations of the electronic structure of the dimer using density functional theory methods, the ORCA program was used [17]. All three types of dimers were calculated $ET_2^+$ without taking into account the crystal field effect. Non-optimized atomic coordinates obtained from X-ray diffraction analysis $\kappa$-(BEDT-TTF)$_2$Cu[N(CN)$_2$]Cl at $T = 280$ K were used as input parameters. Within this calculation, which is more rigorous compared to PMX, the basic characteristics of isolated dimers were refined – the total energy of the electronic system and dipole moments. The relative energies of three different dimer configurations calculated by the DFT method were: $E_{ES} = E_0 + 0.4565$ eV, $E_{SS} = E_0 + 0.91432$ eV, where $E_0 = E_{EE}$, and the effective dipole moments are $\mu_{EE} = 7.3 \cdot 10^{-3}$ D,

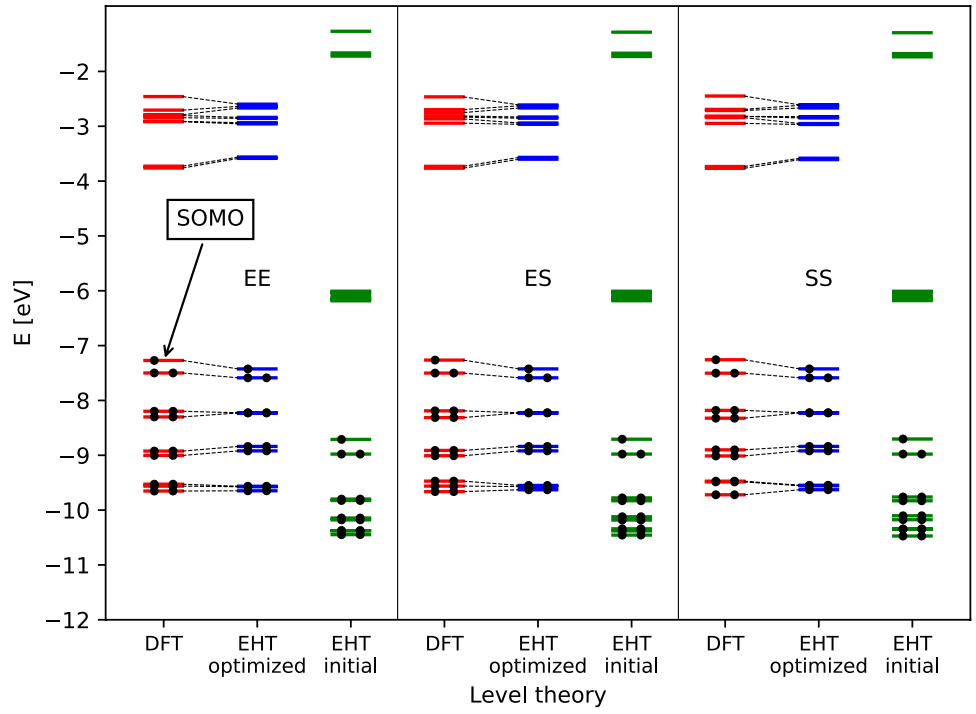


**Fig. 8.** Energy diagrams of molecular levels of dimers $ET_2^+$ in two configurations, calculated using density functional theory methods, standard extended Hückel method, and extended Hückel method with optimized parameters. SOMO – singly occupied molecular orbital of dimer

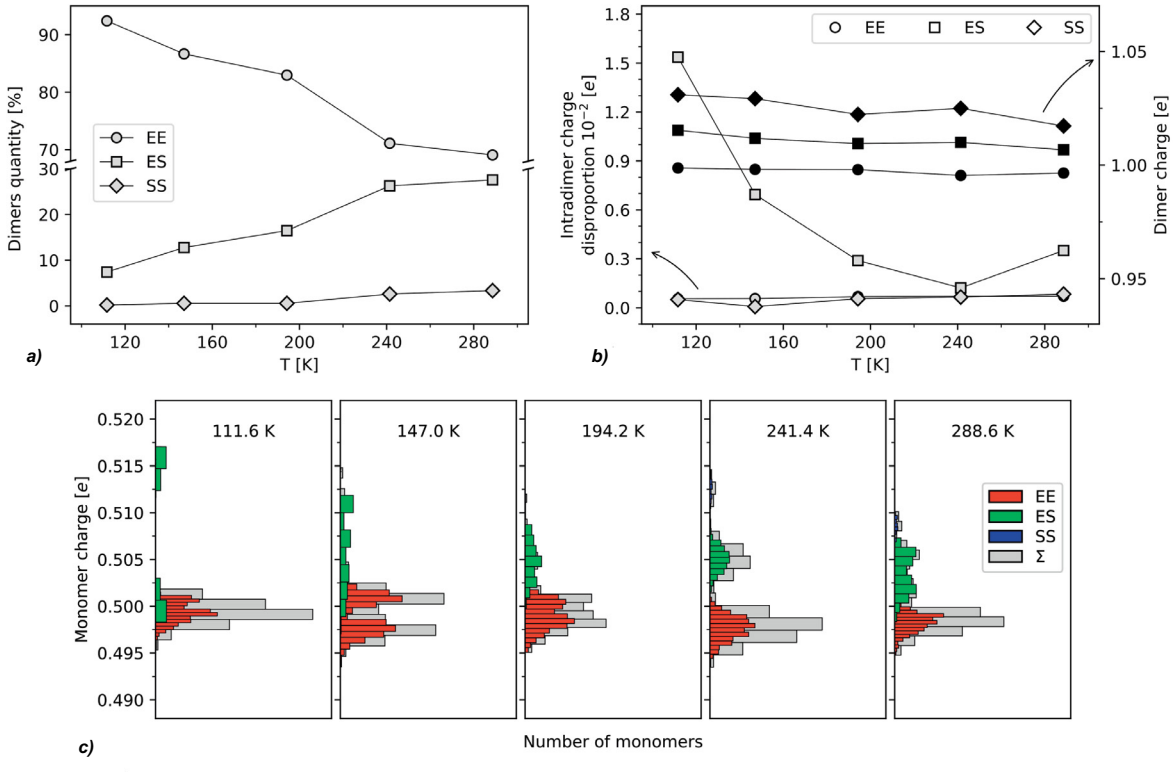


**Fig. 9.** Distribution of charges and dimer types in the conducting layer: percentage of dimers in samples at different temperatures (*a*), average charge of EE, ES, and SS dimers and average charge difference between their monomers (*b*), histograms of monomer charge distribution in the layer (*c*)

$\mu_{ES} = 1.12 \cdot 10^{-1}$D, $\mu_{SS} = 7.1 \cdot 10^{-3}$D (values are given in Debyes, units of molecular dipole moment measurement). Thus, calculations predict that the ES dimer has a dipole moment two orders of magnitude larger than the symmetric dimers EE and SS dimers.

For calculating the electronic characteristics of the disordered cationic ET layer based on structural data, a Monte Carlo method variation was applied, with the following algorithm. For five temperature points, supercells were constructed $3 \times 1 \times 3$ with tripled translation periods along the layer plane. Each of these supercells was replicated to a set of 30 copies with random selection of group configurations $-C_2H_4-$ and strict fulfillment of the condition for the ratio of total E- and S-configurations at a given temperature (see Fig. 5*a*). The final results of calculations were total electronic energies and charge states of molecules, calculated using the Mulliken population analysis [48], and other basic system characteristics. This scheme for calculating corrections to atomic electron density was chosen as the most common among those that take into account matrices of spatial overlap integrals $S_{ij}$ of atomic basis functions $i$ and $j$.

Briefly, the results of modeling charge distribution across dimers are presented in Fig. 9. Considering the set of 30 supercells, the total number of dimers and monomers participating in the analysis for each temperature point equals 540 and 1080 respectively. The relative quantities of dimers in the layer as percentages are shown in Fig. 9*a*. They fully correspond to the populations of E- and S-configurations of ethylene groups obtained from XRD. The curves in Fig. 9*b* and Fig. 9*c* show the averaged values of the total dimer charge and the difference between the minimum and maximum charges of monomers in dimers. It can be seen that in symmetric dimers (with inversion center) EE and SS, the disproportion in charge distribution is small, and the monomers of such dimers are symmetrically charged. In asymmetric dimers of ES type, the situation is different. The disproportion in charge distribution of ES-dimers is present throughout the temperature range, and the redistribution curve itself has a parabolic shape with a minimum at $T = 234$ K. At this temperature, all dimers experience equalization of monomer charges and charge redistribution disappears, although the total dimer charges continue to differ significantly (see Fig. 9*b*). At relatively low temperatures (100–150 K) the difference in monomer charges of the ES dimer is maximal and equals $0.015e$, and the difference in electron density distribution of monomers becomes more evident.

A visual scheme of the charge structure of the conducting ET-layer is presented in Fig. 10*a*. using the temperature point 288.6 K as an example. In the scheme, the sizes of atoms in molecules are proportional to the total molecular charge, which allows visualization of charge redistribution in dimers. It can be seen that compared to EE and SS dimers, mixed composition ES dimers are highly heterogeneous, which corresponds to their higher dipole moment value. EE and SS dimers are uniformly charged, however, SS-dimers show that even under the conditions of the layer's periodic potential, which is applied in the PMX method, the correlation of charge heterogeneities with the DFT calculations of isolated dimers' dipole moments persists. It should be noted that the total layer charge – the sum of atomic charges without averaging over molecules, does not change and is one of the basic fixed calculation parameters.

The combined graph in Fig. 9*c* contains histograms of charge distribution for ET monomers in the conducting layer. The histograms provide the most complete information about the charge structure of the layer; however, their analysis requires additional information about dimer typification. The charge distributions show that most monomers have a charge close to stoichiometric, as they are concentrated in a large maximum slightly below $1/2e$. Comparing the data on dimer concentrations, their average charge and redistribution, we note that this maximum is formed predominantly from EE-type monomers. At a temperature of 194.2 K, the peak begins to broaden slightly, and at 147 K it splits into two narrow maxima. Such splitting is due to some change in the nature of charge redistribution within the monomer and possibly related to the formation of an incommensurate charge superstructure, experimentally observed in some ET-containing layered crystals.

In a sense, the opposite situation is observed for high-temperature distributions. It is necessary to separately consider the histogram at $T = 241.4$ K, as this temperature precedes the region where "anomalies" are observed in increase behavior of structural characteristics (see Fig. 4). The histogram

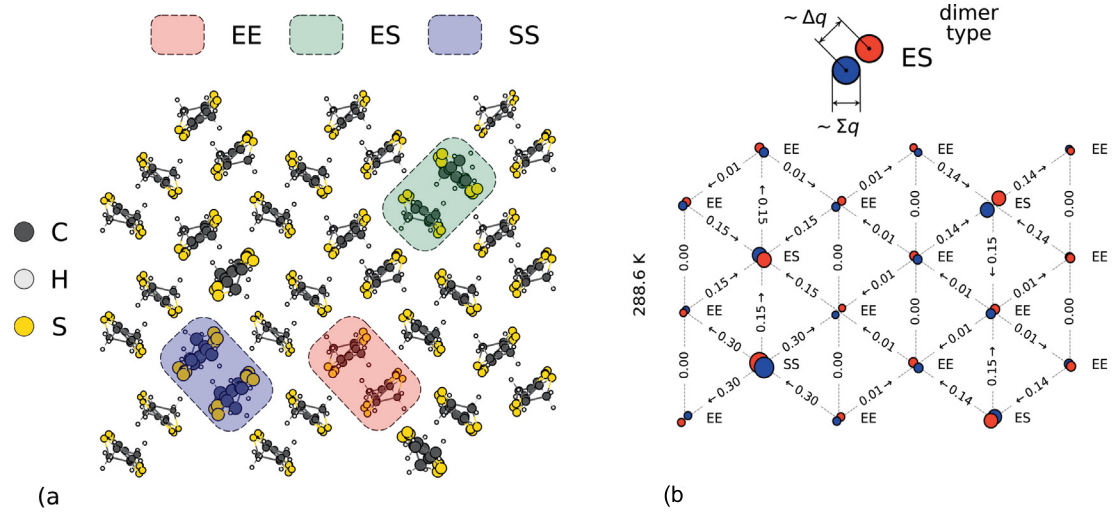


**Fig. 10.** Charge structure of the conducting layer at $T = 288.6$ K (left) and its model representation (right). The figure on the left shows the atomic structure obtained from X-ray structural analysis, except that the sizes of non-hydrogen atoms in each individual molecule are proportional to the total charge on that molecule. The triangular grid in the right figure corresponds to the dimer grid, two circles at the grid node represent two monomers in a dimer, the distance between circles represents the difference in charges of monomers in the dimer $\Delta q$ (dimer polarization), circle size represents the total dimer charge $\sum q$. The blue-red color differentiation of circles corresponds to excess and deficiency of electron density on the monomer. The numbers on the right scheme show the energy difference of the frontal halffilled orbitals (SOMO, see Fig. 8) $\Delta E_{ij} = \left| E_i^{SOMO} - E_j^{SOMO} \right| / 2$ of two adjacent dimers $i$ and $j$ in meV, arrows indicate the direction of SOMO energy

shows three distinct peaks that concentrate monomers of only certain types of dimers: EE (lower, largest peak), ES (middle peak), and SS (upper peak with maximally charged dimers). Consequently, the observed charge inhomogeneities "encompass" the entire dimer, i.e., are bound to a specific node of the triangular sublattice of the layer. It is interesting to note the similarity between the temperature curves of the monomer charge difference ES and the ratio of parameters $a/c \sim t'/t$ (see Fig. 4*b*), which indicates a connection between the geometric parameters of the triangular lattice and the distribution of electron density in the layer.

From the analysis of ET charge distributions, two conclusions can be made. First, the bifurcation of the lower maximum on low-temperature histograms (see Fig. 9*c*) indicates the possible formation of non-trivial charge interactions in the conducting layer during slow cooling, for example, the emergence of states of the so-called quantum dipole crystal. Real cases of such states were previously described in works on comparative analysis of Raman spectra and frequencies of intramolecular vibrations of bonds C = C in samples of some $\kappa$-phases: $\kappa$-(BEDT-TTF)$_2$Hg(SCN)$_2$Cl, $\kappa$-(BEDT-TTF)$_2$Cu$_2$(CN)$_3$ and $\kappa$-(BEDT-TTF)$_2$Hg(SCN)$_2$Br [7]. As applied to to $\kappa$-salts, the essence of this phenomenon lies in changing the types of interacting objects. In an anisotropic triangular layer with strongly polarized dimers, it is necessary to consider electronic interactions between individual ET molecules rather than dimers $ET_2^+$. In this case, the exchange interaction constant $J = 4t^2/U$ ($t$ — transfer integral, and $U$ — electron interaction energy at the site) is multiply reduced compared to $J$ for an isotropic lattice of unpolarized dimers due to the transition $U$ from the energy of magnetic interactions within the dimer to the Coulomb energy of electronic interactions on a single molecule. Theoretical estimates give $J \approx 80$ K for the dipole crystal and $J \approx 250$ K for the Mott insulator with a simple lattice of unpolarized dimers (values given for $\kappa$-(BEDT-TTF)$_2$Cu$_2$(CN)$_3$). The second conclusion is that in a narrow temperature range near the minimum on the ES monomer charge redistribution graph see there are prerequisites for the formation of a state with a triangular anisotropic lattice of weakly polarized dimers, similar to the Mott insulator $\kappa$-(BEDT-TTF)$_2$Cu$_2$(CN)$_3$. In the system of charges distributed according to this type, weakly polarized dimers have different charges, therefore such a system only resembles layers $\kappa$-(BEDT-TTF)$_2$Cu$_2$(CN)$_3$, but does not correspond to them exactly.

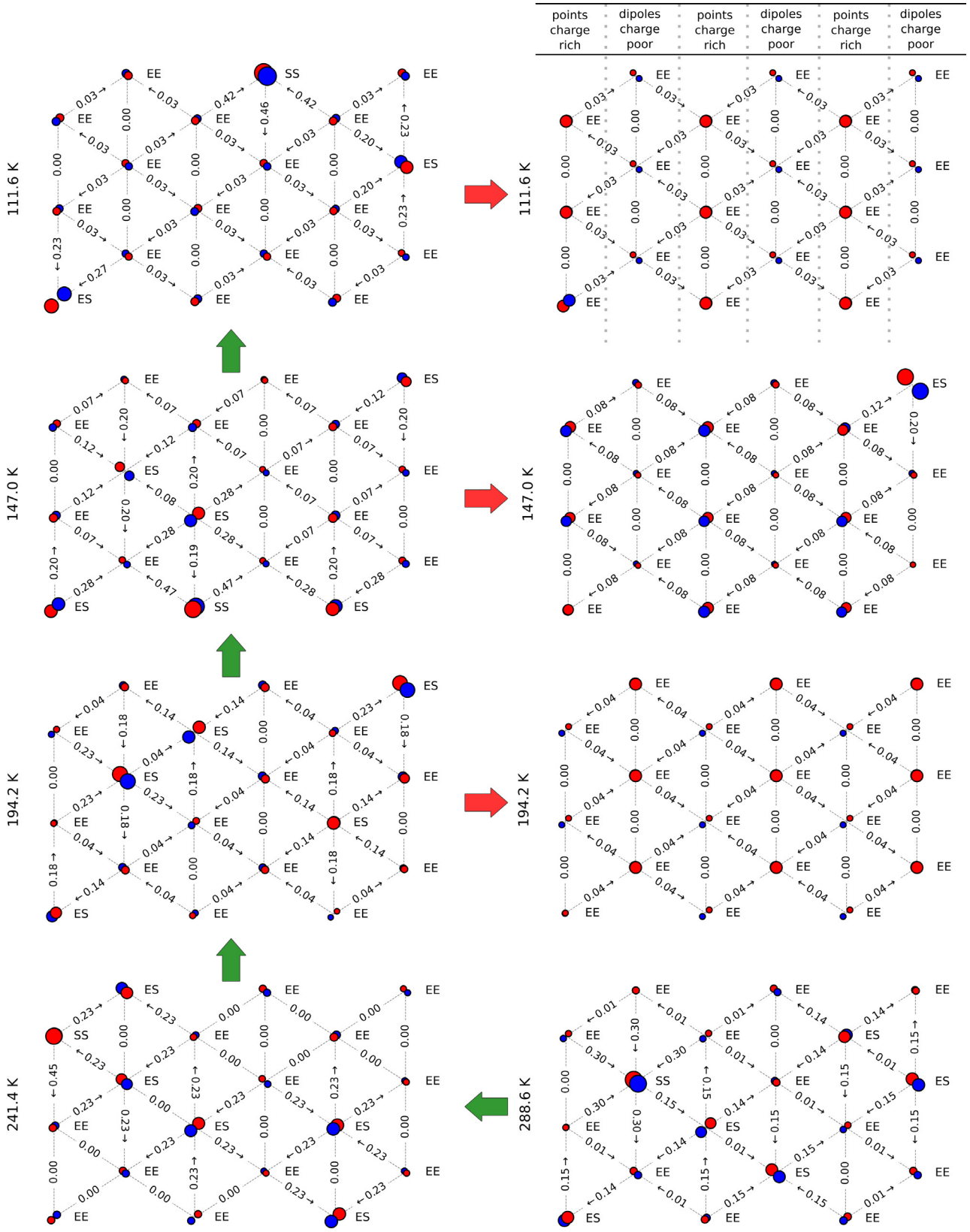


**Fig. 11.** Typical schemes of dimer charge states in the conducting layer at different temperatures. Green arrows show the direction of sequential cooling, red arrows show alternative charge distribution variants if they occur in a particular sample. The values of sizes and displacements of circles in lattice nodes correspond to the description for Fig. 10. When constructing the grid, the values $\Delta q$ and $\sum q$ were normalized to their average values in this layer

The presented analysis of monomer and dimer charges in the layer confirms the stated assumptions and, moreover, predicts the formation of non-trivial charge distribution patterns. Figure 11 shows a diagram of the calculated charge states of ET layers that emerge as dimers of different types are shuffled during slow sample cooling. The charge state here refers to the electron density distribution obtained by solving the problem of minimizing the total electronic energy of the system using optimized PMX. For clarity, when constructing the schemes, the values of monomer charge redistribution and total dimer charges were normalized to their average values in the layer (thus ES dimers for $T = 111.6$ K are polarized much more strongly than ES dimers for $T = 241.4$ K, although they look visually identical). Graphical explanations for constructing layer charge state schemes are presented in Figure 10*b*.

Analysis of the sample shows that in high-temperature structures at $T = 288.6$ K and $T = 241.4$ K, when concentrations of asymmetric ES and "energetically less favorable" SS dimers are high, layers represent a chaotic arrangement of dimers both in relation to the total dimer charge and its degree of polarization. With further temperature decrease, the charge arrangement pattern changes: among multiple chaotic distributions (see green arrows direction in Fig. 11), layers with relatively ordered charge structure begin to appear (see red arrows direction in Fig. 11), with the number of such ordered structures increasing in samples when transitioning from $T = 194.2$ K to $T = 111.6$ K. Thus, in the low-temperature region, two types of distribution can be distinguished: a uniform field of similarly charged EE dimers with single inclusions of recharged SS dimers and polarized ES dimers, or an ordered striped structure of EE dimers. The trigger for switching from one state to another is apparently some critical concentration value of ES and SS dimers, directly related to the residual occupancy value of the minor configuration of ethylene groups.

Special attention should be paid to the low-temperature layers with charge ordering, which are shown in the right panels of Fig. 11. The layers consist of alternating chain-stripes of relatively strongly polarized and weakly polarized EE dimers, which differs from the hypothetical ordered charge structures proposed in the literature, including quantum dipole crystal states [7]. The electron density concentrates in bands with polarized dimers, while weakly polarized bands are positively overcharged – this explains the splitting of the large lower maximum in the low-temperature histograms of Fig. 9. Regardless of the degree of polarization, dimers in each band are charged equally. This leads to the fact that the energies of their singly occupied molecular orbitals (SOMO) are approximately equal, and the half-differences of energies $\Delta E_{ij} = |E_i^{SOMO} - E_j^{SOMO}|/2 = 0$ (see caption to Fig. 10). For systems of identical components, the value $\Delta E_{ij}$ is, to a first approximation, equal to the charge transfer integral between these components [49, 50], consequently, zero values $\Delta E_{ij}$ indicate weak interaction between equally charged dimers within the bands. For dimers of adjacent bands $\Delta E_{ij} > 0$, which causes the redistribution of electron density between bands and corresponds to the directions of charge "flow". Such a striped structure can explain the diffuse transition detected in the magnetic susceptibility and transverse conductivity curves (see Fig. 1), if we assume that only isolated regions of the layer with increased value $\Delta E_{ij}$ can transition to the superconducting state.

## 4. CONCLUSIONS

Analysis of crystal structure details $\kappa$-(BEDT-TTF)$_2$Cu[N(CN)$_2$]Cl, Raman spectra and quantum-chemical modeling of the electronic structure revealed that the features on the temperature dependence graphs of structural parameters in the interval 175–250 K are caused by conformational instability of terminal ethylene groups in the cation layer.

The results of quantum-chemical modeling based on structural data indicate the formation of a non-trivial charge system of dimers in conducting layers, characterized by correlations between the dimer charge and charge redistribution between its monomers with the ET molecule conformation type. The most polarized dimers are those not connected by a center of symmetry, with the degree of polarization depending on temperature and being minimal at the center of the mentioned temperature interval. In the high-temperature region, dimers of different polarization degrees are chaotically arranged within the layer; however, in the lowtemperature region, cases of stable stripe-type charge ordering emerge.

The change in ordering types predetermines the cause of peculiarities in the temperature behavior of structural parameters before and after the interval 175–250 K and allows unambiguous association of experimentally detected deviations in the temperature behavior of charge-sensitive vibrational modes with conformational switching of $-CH_2-CH_2-$ groups. The observed features appear only in the case of extremely slow controlled cooling $r_c = -4$ K/h, when the system passes through near-equilibrium states, and disorder in ethylene groups has time to fully relax. If cooling rates are too high, the feature may not manifest, which explains its absence in transverse conductivity graphs effectively obtained in shock freezing regime $r_c = -120$ K/h.

## FUNDINGS

The experimental part of the work was carried out within the state assignment, registration number AAAA-A17-117121120049-3. Modeling of electronic properties was performed using the National Research University (NRU) HSE supercomputer complex.

## REFERENCES


1. T. G. Prokhorova and E. B. Yagubskii, Russ. Chem. Rev. **86**, 164 (2017).
2. J. M. Williams, A. J. Schultz, U. Geiser et al., Science **252**, 1501 (1972).
3. E. B. Yagubskii, N. D. Kushch, A.V. Kazakova et al., J. Exp. Theor. Phys. Lett. **82**, 93 (2005).
4. V. N. Zverev, A.I. Manakov, S. S. Khasanov et al., Phys. Rev. B **74**, 104504 (2006).
5. Y. Huang, Y. Hu, and S. Ren, Appl. Mater. Today **29**, 101569 (2022).
6. C. Hotta, Phys. Rev. B **82**, 241104 (2010).
7. N. Hassan, S. Cunningham, M. Mourigal et al., Science **360**, 1101 (2018).
8. J. Müller, M. Lang, F. Steglich et al., Phys. Rev. B **65**, 144521 (2002).
9. T. Hiramatsu, Y. Yoshida, G. Saito et al., J. Mater. Chem. C **3**, 1378 (2014).
10. J. Müller, M. Lang, F. Steglich et al., J. De Physique Iv. Proc. **114**, 341 (2004).
11. C. A. Angell, Science **267**, 1924 (1995).
12. F. Gugenberger, R. Heid, C. Meingast et al., Phys. Rev. Lett. **69**, 3774 (1992).
13. T. Komatsu, T. Nakamura, N. Matsukawa et al., Solid State Commun. **80**, 843 (1991).
14. G. M. Sheldrick, Acta Crystallogr Sect. Found Adv. **71**, 3 (2015).
15. G. M. Sheldrick, Acta Crystallogr Sect. C Struct. Chem. **71**, 3 (2015).
16. H. J. Monkhorst and J. D. Pack, Phys. Rev. B **13**, 5188 (1976).
17. F. Neese, Wiley Interdiscip. Rev. Comput. Mol. Sci. **2**, 73 (2012).
18. R. Ditchfield, W. J. Hehre and J. A. Pople, J. Chem. Phys. **54**, 724 (1971).
19. Y. Saito, A. Löhle, A. Kawamoto et al., Crystals **11**, 817 (2021).
20. D. Cvijović, Theor. Math. Phys. **166**, 37 (2011).
21. D. P. Shoemaker, D. Y. Chung, H. Claus et al., Phys. Rev. B **86**, 184511 (2012).
22. J. M. Williams, A. M. Kini, H. H. Wang et al., Inorg. Chem. **29**, 3272 (1990).
23. Y. V. Sushko, V. A. Bondarenko, R. A. Petrosov et al., J. Phys. II **1**, 1015 (1991).
24. H. O. Jeschke, M. de Souza, R. Valentí et al., Phys. Rev. B **85**, 035125 (2012).
25. C. G. Darwin, Philos. Mag. Ser. 6 **43**, 800 (1922).
26. E. Arnold and D. M. Himmel, *International Tables for Crystallography Volume F: Crystallography of Biological Macromolecules,* John Wiley & Sons Ltd., (2011).
27. D. H. Juers, C. A. Farley, C. P. Saxby et al., Acta Crystallogr. Sect. D **74**, 922 (2018).
28. D. H. Juers, J. Lovelace, H. D. Bellamy et al., Acta Crystallogr. Sect. D **63**, 1139 (2007).
29. A. Vahedi-Faridi, J. Lovelace, H. D. Bellamy et al., Acta Crystallogr. Sect. D **59**, 2169 (2003).
30. U. Shmueli, *International Tables for Crystallography. Volume B: Reciprocal Space*, Springer (2001).
31. K. Miyagawa, A. Kawamoto, Y. Nakazawa et al., Phys. Rev. Lett. **75**, 1174 (1995).
32. M. A. Tanatar, T. Ishiguro, T. Kondo et al., Phys. Rev. B **59**, 3841 (1999).
33. P. Wzietek, H. Mayaffre, D. Jerome et al., J. Phys. **6**, 2011 (1996).
34. P. Wzietek, H. Mayaffre, D. Jerome et al., Synthetic Met. **85**, 1511 (1997).
35. X. Su, F. Zuo, J. A. Schlueter et al., Phys. Rev. B **57**, R14056 (1998).
36. S. Yasin, M. Dumm, B. Salameh et al., Eur. Phys. J. B **79**, 383 (2011).
37. P. Nagel, V. Pasler, C. Meingast et al., Phys. Rev. Lett. **85**, 2376 (2000).

**38.** T. Yamamoto, M. Uruichi, K. Yamamoto et al., J. Phys. Chem. B **109**, 15226 (2005).

**39.** K. Yakushi, Crystals **2**, 1291 (2012).

**40.** H. H. Wang, J. R. Ferraro, J. M. Williams et al., J. Chem. Soc., Chem. Commun., 1893 (1994).

**41.** I. Olejniczak, B. Barszcz, P. Auban-Senzier et al., J. Phys. Chem. C **126**, 1890 (2022).

**42.** L. A. Hess and P. N. Prasad, J. Chem. Phys. 72, 573 (1980).

**43.** S. Tomić, M. Pinterić, T. Ivek et al., J. Phys.: Condens. Matter **25**, 436004 (2013).

**44.** L. A. Girifalco, *Statistical Mechanics of Solids*, Oxford University Press, (2000).

**45.** L. Bellaiche and D. Vanderbilt, Phys. Rev. B **61**, 7877 (2000).

**46.** P. Soven, Phys. Rev. **156**, 809 (1967).

**47.** G. Landrum, YAeHMOP 3.0 (2023).

**48.** R. S. Mulliken, J. Chem. Phys. **23**, 1833 (1955).

**49.** H. Nishioka and K. Ando, J. Chem. Phys. **134**, 1 (2011).

**50.** A. Biancardi, S. C. Martin, C. Liss et al., J. Chem. Theory Comput. **13**, 4154 (2017).